

# MLS-based SPH in LS-DYNA<sup>®</sup> for Increased Accuracy and Tensile Stability

Edouard Yreux  
Livermore Software Technology Corporation

## Abstract

*Two important limitations of the Smoothed Particle Hydrodynamics are low accuracy and tensile instability. While the former can be somewhat alleviated by employing very fine discretizations and renormalized formulations, the latter can only be slightly mitigated with heavy use of artificial viscosity. In addition, renormalized formulations can be unsuitable for extreme deformations and impact simulations, and excessive artificial viscosity can severely alter the physics of the problem being modeled. A new formulation based on a Moving Least-Squares approximation and an improved nodal integration scheme is presented in this paper. The method is shown to be much more stable in tension, and very accurate. Extensive comparisons with traditional SPH and with experimental data are presented.*

## Introduction

The Smoothed Particle Hydrodynamics (SPH) method [1,2] provides an interesting alternative to traditional finite element methods for numerical simulations involving impact, material fragmentation, or very large deformations. Common issues that arise when modeling this kind of events, such as mesh entanglement, element distortion or inversion are avoided by the meshfree nature of the method. However, SPH suffers from well-known tensile instability issues [3] that are difficult to resolve, poor convergence properties [4], and low accuracy.

In this paper, we introduce the MLS-Based formulation recently implemented in the SPH module of LS-DYNA. The main equations of the traditional SPH formulation are presented first, followed by the theory and LS-DYNA implementation of the MLS-Based formulation. Some numerical examples and comparisons between formulations are provided next, along with comparisons with available experimental data. The new formulation is shown to have much better stability in tension, better overall accuracy, and better agreement with experiment in validation tests.

## Standard SPH Formulation

The main theory and derivation of the SPH method has already been well documented, therefore only the main equations are recalled below. For a more in-depth review of the theoretical foundation, see for example [5]. The heart of the method relies on interpolation theory. Namely, for a function  $f$  defined over a domain  $\Omega$ , and for  $\mathbf{x} \in \Omega$ , we define the interpolation  $\langle f \rangle$  as:

$$\langle f(\mathbf{x}) \rangle = \int_{\Omega} f(\mathbf{y}) W(|\mathbf{x} - \mathbf{y}|/h) d\mathbf{y}, \quad (1)$$

where  $W$  is a kernel function of support determined by the parameter  $h$ . A common choice for  $W$  is the cubic B-spline function, which is the default kernel available in LS-DYNA. After discretization, this interpolation evaluated at particle  $I$  is approximated as

$$\langle f(\mathbf{x}_I) \rangle \approx \sum_J \frac{m_J}{\rho_J} f(\mathbf{x}_J) W(|\mathbf{x}_I - \mathbf{x}_J|/h), \quad (2)$$

where  $\mathbf{x}_J$ ,  $m_J$  and  $\rho_J$  are the position, mass and density associated with particle  $J$ , respectively. The discretized continuity and momentum conservation equations in SPH are generally expressed as

$$\frac{d\rho_I}{dt} = \rho_I \sum_J \frac{m_J}{\rho_J} (\mathbf{v}_J - \mathbf{v}_I) \cdot \nabla W_{IJ} \quad (3)$$

and

$$\frac{d\mathbf{v}_I}{dt} = - \sum_J m_J \left( \frac{\boldsymbol{\sigma}_I}{\rho_I^2} + \frac{\boldsymbol{\sigma}_J}{\rho_J^2} \right) \cdot \nabla W_{IJ}, \quad (4)$$

where  $\boldsymbol{\sigma}_I$  is the stress tensor at particle  $I$  in Voigt notation,  $\mathbf{v}_I$  is the velocity at particle  $I$ , and  $\nabla W_{IJ} = \nabla W(|\mathbf{x} - \mathbf{x}_J|/h)|_{\mathbf{x}=\mathbf{x}_I}$  is the gradient of the kernel function associated with particle  $J$  evaluated at particle  $I$ .

While simple to implement and extremely robust, the traditional SPH suffers from relatively poor accuracy. Though this can be somewhat alleviated by using kernel gradient correction techniques [6, 7] to improve completeness, Figure 1 illustrates how a simple wave propagation problem is still difficult to capture for this method. Some known stability issues [3] also require the use of artificial viscosity, which adds undesirable numerical dissipation. As illustrated in a numerical example in section 4, tensile instability causes particles to break apart prematurely, widely limiting the reliability of numerical results obtained with SPH methods for problems involving tension.

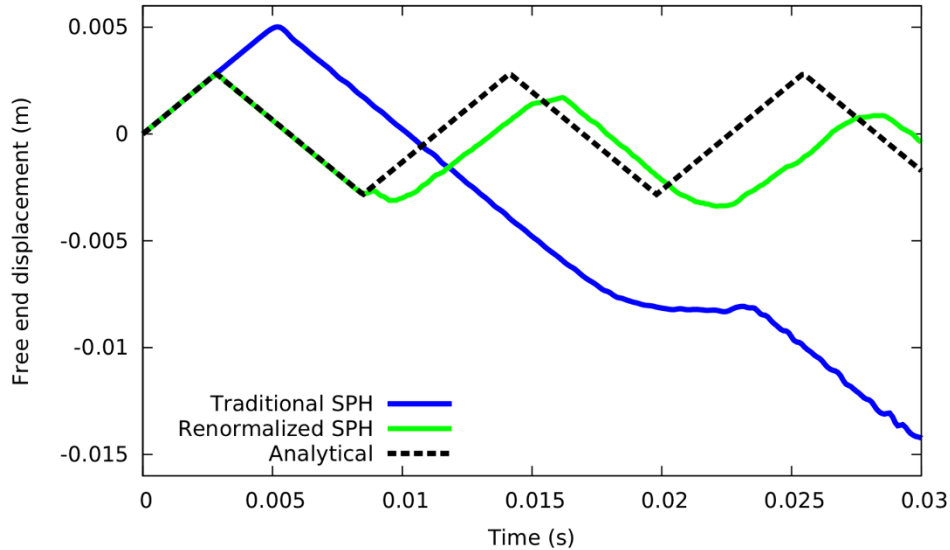


Figure 1: Longitudinal wave propagating in a 1D bar modeled with SPH and renormalized SPH, compared to analytical solution.

## Moving Least-Squares Based Formulation

### Method derivation

The method is based on two techniques derived in the Reproducing Kernel Particle Method (RKPM)[8] framework. A quasi-linear least-squares construction is employed as approximation functions [9], replacing the SPH kernel functions. The continuity and momentum equations presented in the previous section are replaced by a stabilized and nodally integrated weak-form [10]. Only a brief summary of both methods is presented here, as a thorough derivation can be found in both papers.

We now consider a two-dimensional case, though the results are directly applicable to 3-D and 1-D formulations. We first introduce the following notations.  $\mathbf{H}$  is a vector of monomials defined as

$$\mathbf{H}(\mathbf{x} - \mathbf{x}_I) = \begin{bmatrix} 1 & x - x_I & y - y_I \end{bmatrix}, \quad (5)$$

and the corresponding moment matrix  $\mathbf{M}(\mathbf{x})$  is expressed as

$$\mathbf{M}(\mathbf{x}) = \sum_{I=1}^{N_P} \mathbf{H}(\mathbf{x} - \mathbf{x}_I) \mathbf{H}^T(\mathbf{x} - \mathbf{x}_I) W(|\mathbf{x} - \mathbf{x}_I|/h). \quad (6)$$

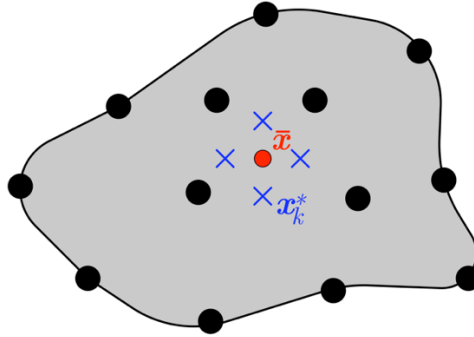


Figure 2: Example of sampling points  $\{\mathbf{x}_k^*(\bar{\mathbf{x}})\}$  in a two-dimensional domain.

The traditional first order RKPM approximation function, based on a moving least-squares construction, is written as [11]

$$\Psi_I^R(\mathbf{x}) = \mathbf{H}^T(\mathbf{0}) \mathbf{M}^{-1}(\mathbf{x}) \mathbf{H}(\mathbf{x} - \mathbf{x}_I) W(|\mathbf{x} - \mathbf{x}_I|/h). \quad (7)$$

To circumvent possible singularity of the moment matrix defined in (6) when particles spread apart, quasi-linear reproducing functions [9] are used instead. A coefficient  $\alpha > 0$  is introduced. For any  $\bar{\mathbf{x}} \in \Omega$ , consider a set of sampling points  $\{\mathbf{x}_k^*(\bar{\mathbf{x}})\}_{k=1}^4$  not contained on a line, as illustrated in Figure 2. The quasi-linear approximation function is defined as

$$\Psi_I(\mathbf{x}) = \mathbf{H}^T(\mathbf{0}) \tilde{\mathbf{M}}^{-1}(\mathbf{x}) \tilde{\mathbf{H}}(\mathbf{x}, \mathbf{x}_I) W(|\mathbf{x} - \mathbf{x}_I|/h), \quad (8)$$

with

$$\tilde{H}(\mathbf{x}, \mathbf{x}_I) = H(\mathbf{x} - \mathbf{x}_I) + \alpha \sum_{k=1}^{N_S} H(\mathbf{x} - \mathbf{x}_k^*(\mathbf{x})) \quad (9)$$

and

$$\tilde{M}(\mathbf{x}) = M(\mathbf{x}) + \alpha M^*(\mathbf{x}), \quad (10)$$

where

$$M^*(\mathbf{x}) = \sum_{I=1}^{N_P} \sum_{k=1}^{N_S} H(\mathbf{x} - \mathbf{x}_k^*(\mathbf{x})) H^T(\mathbf{x} - \mathbf{x}_k^*(\mathbf{x})) W(|\mathbf{x} - \mathbf{x}_I|/h). \quad (11)$$

The modified moment matrix defined in (10) can easily be shown as non-singular for any position of neighboring particles, greatly increasing the robustness of the approximation. A more thorough investigation of the approximation properties of the method can be found in [9].

The continuity and momentum conservation equations in (3) and (4) are replaced by the following expressions:

$$\frac{d\rho_I}{dt} = \rho_I \sum_J \mathbf{v}_J \cdot \nabla \Psi_J(\mathbf{x}_I) \quad (12)$$

and

$$m_I \frac{d\mathbf{v}_I}{dt} = \sum_J \mathbf{B}_I^T(\mathbf{x}_J) \boldsymbol{\sigma}_J V_I + \mathbf{f}_I^{\text{stab}}, \quad (13)$$

where  $\boldsymbol{\sigma}_J$  is the stress tensor at particle  $J$  in Voigt notation,  $V_I$  is the volume associated with particle  $I$ , and

$$\mathbf{B}_I(\mathbf{x}) = \begin{bmatrix} \Psi_{I,x}(\mathbf{x}) & 0 \\ 0 & \Psi_{I,y}(\mathbf{x}) \\ \Psi_{I,y}(\mathbf{x}) & \Psi_{I,x}(\mathbf{x}) \end{bmatrix}. \quad (14)$$

The stabilization term in (13) associated with particle  $I$ ,  $f_I^{\text{stab}}$ , is calculated as [10]

$$\mathbf{f}_I^{\text{stab}} = \sum_J \left[ \mathbf{B}_{Jx}^T(\mathbf{x}_I) \boldsymbol{\varsigma}_{Jx}^s M_{Jx} + \mathbf{B}_{Jy}^T(\mathbf{x}_I) \boldsymbol{\varsigma}_{Jy}^s M_{Jy} \right], \quad (15)$$

with

$$\mathbf{B}_{Ix}(\mathbf{x}) = \begin{bmatrix} \Psi_{I,xx}(\mathbf{x}) & 0 \\ 0 & \Psi_{I,xy}(\mathbf{x}) \\ \Psi_{I,xy}(\mathbf{x}) & \Psi_{I,xx}(\mathbf{x}) \end{bmatrix}, \quad \mathbf{B}_{Iy}(\mathbf{x}) = \begin{bmatrix} \Psi_{I,xy}(\mathbf{x}) & 0 \\ 0 & \Psi_{I,yy}(\mathbf{x}) \\ \Psi_{I,yy}(\mathbf{x}) & \Psi_{I,xy}(\mathbf{x}) \end{bmatrix}, \quad (16)$$

$$\boldsymbol{\varsigma}_{Ix}^s = C_I \sum_J \mathbf{B}_{Jx}(\mathbf{x}_I) \mathbf{v}_J, \quad \boldsymbol{\varsigma}_{Iy}^s = C_I \sum_J \mathbf{B}_{Jy}(\mathbf{x}_I) \mathbf{v}_J. \quad (17)$$

where  $\mathbf{C}_I$  is the material consistent tangent at particle  $I$ .  $M_{Ix}$  and  $M_{Iy}$  are the second moments of area of a representative volume around particle  $I$  in the  $x$  and  $y$  directions, respectively. For better CPU efficiency, the first order derivatives in (14) are approximated via a smoothed gradient operator [12]. The second order derivatives in (16) are approximated via an implicit gradient expansion [13, 10] operating on the first order derivatives obtained from the aforementioned smoothed gradient operation.

## Implementation in LS-DYNA

This formulation was integrated in the SPH module of LS-DYNA as a new option in the `*Control_SPH` keyword, by setting `FORM = 12`.

Still using a two-dimensional domain for illustration purposes, the sampling points introduced in section 3.1 are chosen as:

$$\begin{aligned} \mathbf{x}_1^*(\mathbf{x}) &= \{x - \varepsilon h \quad y\} & \mathbf{x}_3^*(\mathbf{x}) &= \{x \quad y - \varepsilon h\} \\ \mathbf{x}_2^*(\mathbf{x}) &= \{x + \varepsilon h \quad y\} & \mathbf{x}_4^*(\mathbf{x}) &= \{x \quad y + \varepsilon h\}. \end{aligned}$$

with  $\varepsilon = 0.05$ , which seems to give good results for a variety of test problems. The parameter  $\alpha$  defined earlier has a default value of  $\alpha = 0.01$  which also seems to be a good balance between stability and accuracy. This value can be modified using the `QL` parameter in `*Control_SPH`, for experimentation. Lower values will slightly improve accuracy, but may trigger instabilities in very large deformations regimes. Conversely, higher values will yield lower accuracy, but can provide greater stability in very large deformations problems.

The default stabilization term in (15) is based on the current stress gradients. This term can optionally be calculated based on the accumulated stress gradients by setting `ISTAB = 1` in `*Control_SPH`. This is only recommended for hyperelastic materials or elasto-plastic materials with hardening, and should not be used for materials with softening or damage.

## Numerical Examples

### Tensile Test

One of the main limitations of the SPH method is the tensile instability mentioned in section 2. To illustrate the problem, consider an elasto-plastic bar under tension as shown in Figure 3a. Both traditional and renormalized SPH formulations result in very early splitting of the bar (Figure 3b, Figure 3c) instead of developing tensile stresses and deformations. The MLS-based formulation however is much less sensitive to this instability, as shown in Figure 3d.

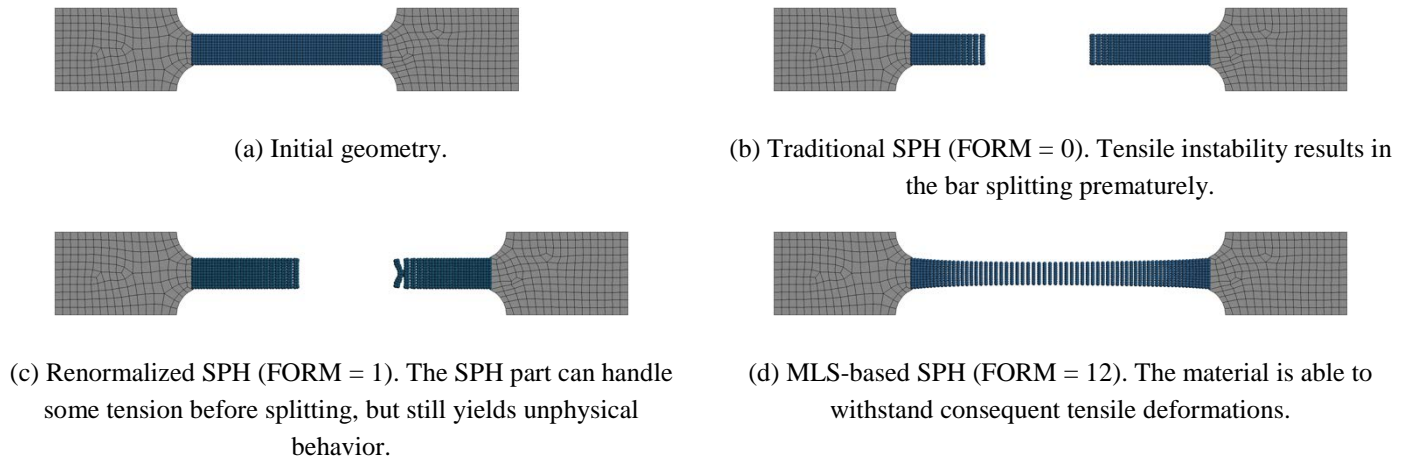


Figure 3: Tensile test problem: The left grip is fixed, while the right grip has a prescribed constant velocity.

## Wave Propagation

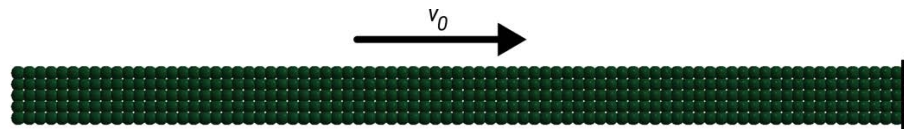


Figure 4: Wave propagation problem, boundary and initial conditions.

In this example, we model an elastic rod of length  $L = 20$  cm and of cross-section  $1 \text{ cm} \times 1 \text{ cm}$  with a free boundary condition at  $x = L$ , a fixed boundary condition at  $x = 0$ , and an initial velocity of  $v_0 = 1 \text{ m} \cdot \text{s}^{-1}$ . The discretization is shown in Figure 4. The material has a density of  $\rho = 2000 \text{ kg}$ , a Young's modulus of  $E = 10 \text{ MPa}$  and a Poisson's ratio of  $\nu = 0.0$ . The longitudinal displacement at the free end is obtained using different methods and compared to the analytical solution, as shown in Figure 6. The analytical displacement at any longitudinal coordinate of the bar is given as

$$u(x, t) = \sum_{k=1}^{\infty} \frac{8(-1)^{k+1}}{\pi^2(2k-1)^2} \frac{v_0 L}{c} \sin\left(\left(2k-1\right)\frac{c\pi}{2L}t\right) \cos\left(\left(2k-1\right)\frac{\pi}{2L}x\right), \quad (18)$$

where  $c = E/\rho$ . The traditional SPH formulation (FORM = 0) yields an incorrect wave speed, and also suffers from tensile instability: as the initial compression wave bounces back to a tension wave, the bar separates into two components, as illustrated in Figure 5. With the renormalized formulation (FORM = 1), tensile instability is still present, but attenuated enough that the bar remains as one component. The accuracy is still quite poor, as illustrated by the incorrect wave period and amplitude shown in Figure 6. By contrast, the MLS-based formulation (FORM = 12) shows good agreement with the analytical solution, both in terms of period and amplitude of displacement, and coincides very well with the expected displacement derived in (18).



Figure 5: Using a traditional SPH formulation, tensile instability allows the material to separate instead of developing tensile stress

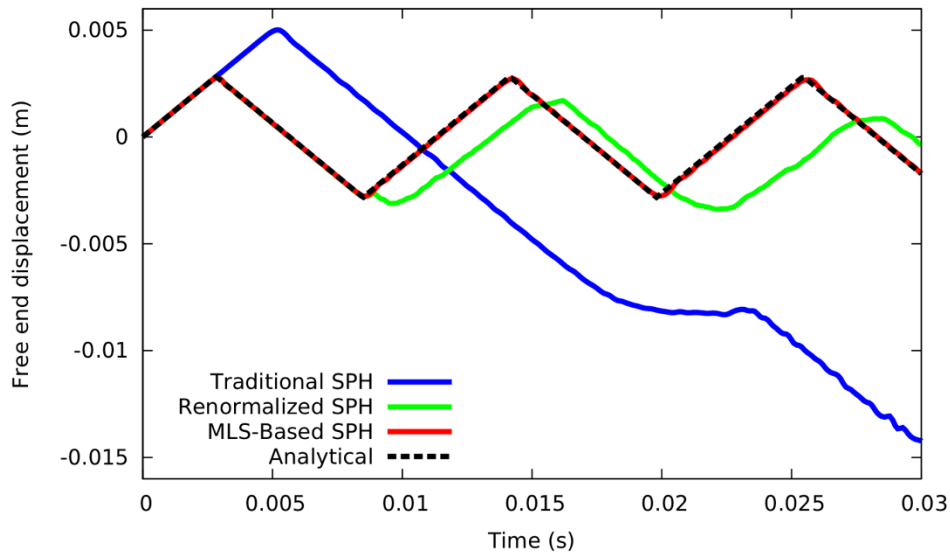


Figure 6: Longitudinal wave propagating in a 1D bar modeled with SPH, renormalized SPH and MLS-Based SPH, compared to analytical solution.

### Aluminum Sphere Impact Simulation

A 1.27 mm thick aluminium alloy 6061-T6 plate is impacted by a S2 tool steel spherical projectile of diameter 7.9 mm. Experimental data and a reference numerical simulation are presented in [14], along with material parameters for both the projectile and the plate. The ballistic limit is determined experimentally to be between  $v_{bl0} = 128 \text{ m}\cdot\text{s}^{-1}$  and  $v_{bl1} = 146 \text{ m}\cdot\text{s}^{-1}$ . An illustration of the discretization employed and of the plate deformations during impact is presented in Figure 7. Figure 8 shows the obtained residual projectile velocity vs. impact velocity with SPH and MLS-Based SPH, compared to the reference simulation and the Recht-Ipson model [15] prediction. Since the ballistic limit is only identified as a range, the Recht-Ipson model is presented as an area in Figure 8. The traditional SPH formulation exhibits a very brittle behavior, likely due to tensile instability. This results in the material fracturing before dissipating energy through plastic deformations, and ultimately largely under-predicting the ballistic limit. The MLS-Based SPH on the other hand slightly overpredicts the ballistic limit, but overall agrees quite well with both the Recht-Ipson model and the results from the OTM simulation by Li et al. [14].

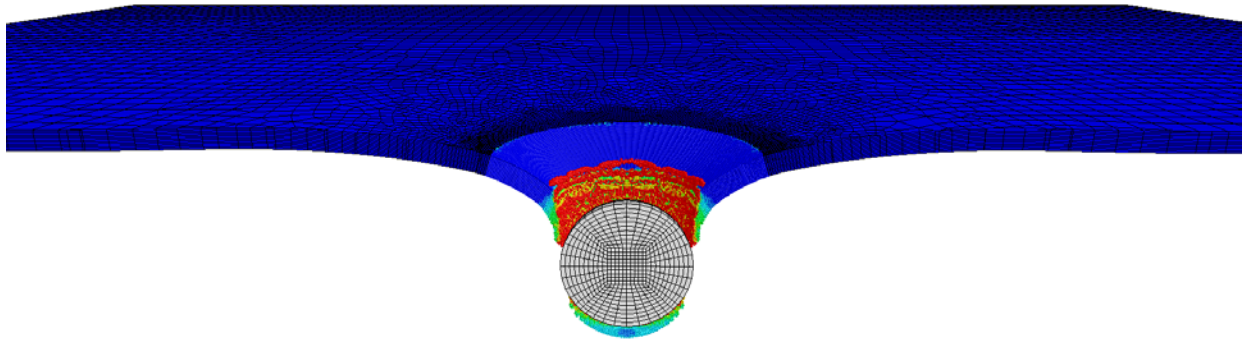


Figure 7: Aluminum impact simulation: Cross-section of the deformed shape during impact.

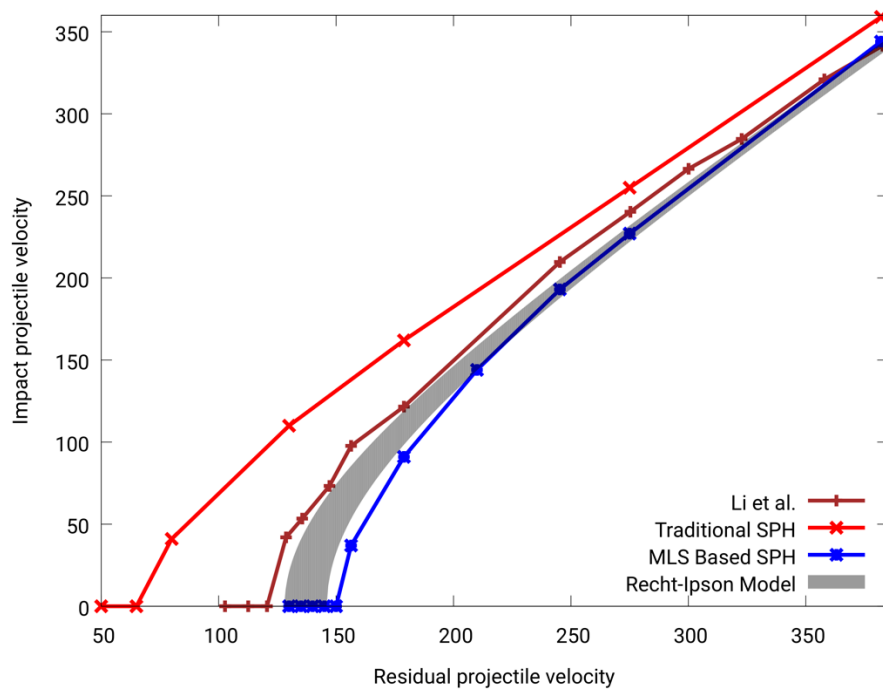


Figure 8: Residual projectile velocity vs. impact velocity with SPH and MLS-Based SPH, compared to reference simulation [14] and Recht-Ipson model.

### Blunt Steel Projectile Impact Simulation

A 12 mm thick Weldox 460E steel plate is impacted by an Arne tool steel cylindrical projectile traveling at  $303.5\text{m}\cdot\text{s}^{-1}$ . The same simulation is carried with the traditional SPH method and with the present method. Detailed experimental data is available in [16], such as projectile exit velocity, plug mass and plug exit velocity, for example. The material has also been characterized and material parameters were identified in [17] for a modified Johnson-Cook material model. Figure 9 shows a cross-section of the simulation after impact, with both traditional SPH and MLS-Based. A qualitative comparison already shows important differences, both in the crater shape prediction and in the resulting plug after impact. A comparison of the velocity history of the projectile with the experimental final velocity is shown in Figure 10, and a table comparing various quantities of interest to this simulation is presented in Table 1, along with relative errors. The higher accuracy of the proposed method is evident, showing better agreement with experimental data on all variables studied in this problem.

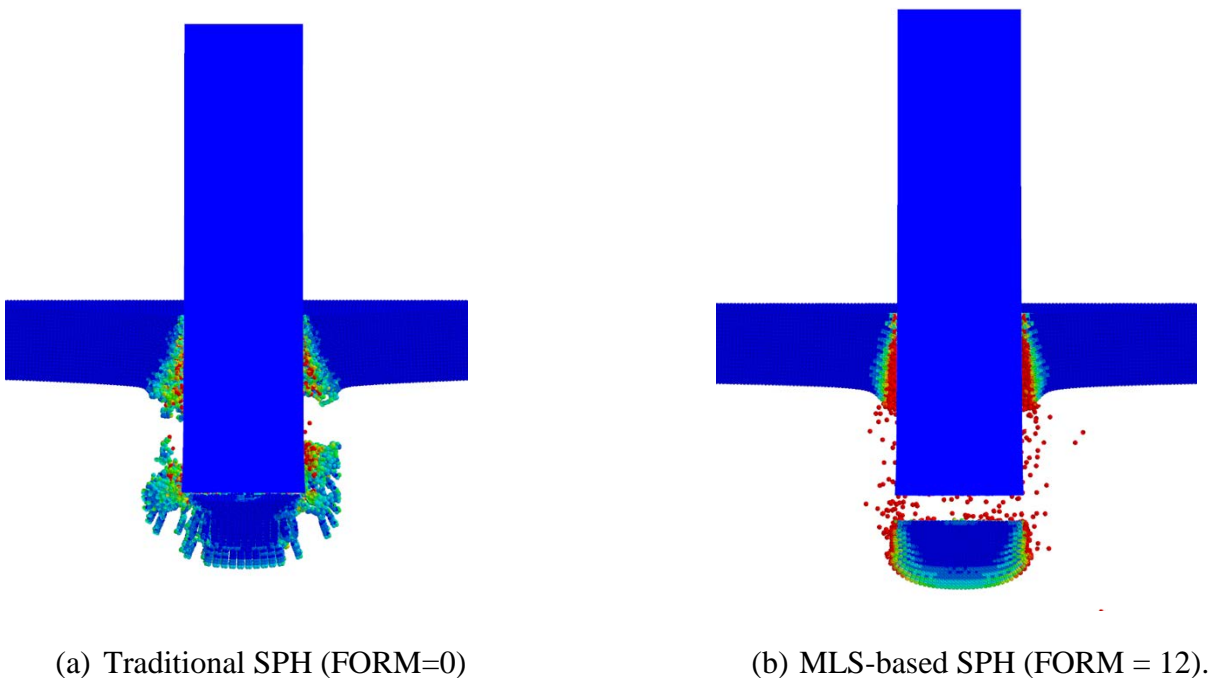


Figure 9: Steel impact simulation after perforation, cross-section view.

Comparison With Experimental Data					
	Experimental	Form 0		Form 12	
Projectile Residual Velocity	199.7 m/s	207.9 m/s	<b>3.9%</b>	201.6 m/s	<b>0.9%</b>
Plug Residual Velocity	242.3 m/s	212 m/s	<b>12.5%</b>	248 m/s	<b>2.4%</b>
Plug Mass	27.6 g	35.9 g	<b>23.1%</b>	28.9 g	<b>4.7%</b>
Plug Height	11.4 mm	17.6 mm	<b>54.4%</b>	11.3 mm	<b>0.9%</b>
Crater, front diameter	20.7 mm	20.4 mm	<b>1.4%</b>	20.6 mm	<b>0.5%</b>
Crater, exit diameter	20.9 mm	30.8 mm	<b>47.4%</b>	23.7 mm	<b>13.4%</b>

Table 1: Comparison between experimental data, traditional SPH and MLS-Based SPH for different variables of interest. Relative errors between numerical method and experiment are also provided.

## Conclusion

A new SPH formulation has been implemented in LS-DYNA, greatly alleviating tensile instability issues and enhancing accuracy. The improved performance of the method was illustrated through simple examples, and a series of impact simulations was presented to validate the implementation. As opposed to fully Lagrangian formulations implemented in LS-DYNA (forms 7 and 8), this new framework provides great stability and accuracy while still being robust to extreme deformations and material fragmentation, as illustrated in the perforation simulation.

## References

- [1] Leon B Lucy. "A numerical approach to the testing of the fission hypothesis". In: *The astronomical journal* 82 (1977).
- [2] R. A. Gingold and J. J. Monaghan. "Smoothed particle hydrodynamics: theory and application to non-spherical stars". In: *Monthly Notices of the Royal Astronomical Society* 181.3 (1977).
- [3] J.W. Swegle, D.L. Hicks, and S.W. Attaway. "Smoothed Particle Hydrodynamics Stability Analysis". In: *Journal of Computational Physics* 116.1 (1995).
- [4] Qirong Zhu, Lars Hernquist, and Yuexing Li. "Numerical convergence in smoothed particle hydrodynamics". In: *The Astrophysical Journal* 800.1 (2015).
- [5] P.W. Randles and L.D. Libersky. "Smoothed Particle Hydrodynamics: Some recent improvements and applications". In: *Computer Methods in Applied Mechanics and Engineering* 139.14 (1996).
- [6] Gordon R Johnson and Stephen R Beissel. "Normalized smoothing functions for SPH impact computations". In: *International Journal for Numerical Methods in Engineering* 39.16 (1996).
- [7] T. Belytschko et al. "On the completeness of meshfree particle methods". In: *International Journal for Numerical Methods in Engineering* 43.5 (1998).
- [8] Wing Kam Liu, Sukky Jun, and Yi Fei Zhang. "Reproducing kernel particle methods". In: *International Journal for Numerical Methods in Fluids* 20.8-9 (1995).
- [9] Edouard Yreux and Jiun-Shyan Chen. "A quasi-linear reproducing kernel particle method". In: *International Journal for Numerical Methods in Engineering* 109.7 (2017).
- [10] Michael Hillman and Jiun-Shyan Chen. "An accelerated, convergent, and stable nodal integration in Galerkin meshfree methods for linear and nonlinear mechanics". In: *International Journal for Numerical Methods in Engineering* (2015).
- [11] Jiun-Shyan Chen et al. "Reproducing Kernel Particle Methods for large deformation analysis of non-linear structures". In: *Computer Methods in Applied Mechanics and Engineering* 139.1 (1996).
- [12] Jiun-Shyan Chen et al. "A stabilized conforming nodal integration for Galerkin mesh-free methods". In: *International Journal for Numerical Methods in Engineering* 50.2 (2001).
- [13] Shaofan Li and Wing Kam Liu. "Reproducing kernel hierarchical partition of unity, Part I: formulation and theory". In: *International Journal for Numerical Methods in Engineering* 45.3 (1999).
- [14] B. Li et al. "Verification and validation of the Optimal Transportation Meshfree (OTM) simulation of terminal ballistics". In: *International Journal of Impact Engineering* 42 (2012).
- [15] R. F. Recht and T. W. Ipson. "Ballistic Perforation Dynamics". In: *Journal of Applied Mechanics* 30.3 (1963). 10
- [16] T Borvik et al. "Perforation of 12 mm thick steel plates by 20 mm diameter projectiles with flat, hemispherical and conical noses: Part I: Experimental study". In: *International Journal of Impact Engineering* 27.1 (2002).
- [17] T. Borvik et al. "Perforation of 12 mm thick steel plates by 20 mm diameter projectiles with flat, hemispherical and conical noses: Part II: numerical simulations". In: *International Journal of Impact Engineering* 27.1 (2002).